CHEMISTRY OF MATERIALS

Article

pubs.acs.org/cm

Analysis of Charged State Stability for Monoclinic $LiMnBO_3$ Cathode

Jae Chul Kim,[†] Xin Li,[†] Charles J. Moore,[†] Shou-Hang Bo,[‡] Peter G. Khalifah,[‡,§] Clare P. Grey,[‡,∥] and Gerbrand Ceder*[,†]

[†]Department of Materials Science and Engineering, Massachusetts Institute of Technology, Cambridge, Massachusetts 02139, United States

[‡]Department of Chemistry, Stony Brook University, Stony Brook, New York 11794, United States

[§]Department of Chemistry, Brookhaven National Laboratory, Upton, New York 11973, United States

[∥]Department of Chemistry, University of Cambridge, Lensfield Road, Cambridge, CB2 1EW, United Kingdom

Supporting Information

ABSTRACT: The stability of the charged state of monoclinic $LiMnBO_3$ has been analyzed to better understand its electrochemical cycling behavior in this work. First-principles calculations indicate that delithiated monoclinic $Li_{1-x}MnBO_3$ becomes unstable for $x \geq 0.625$. Results obtained from *ex-situ* X-ray diffraction on charged electrodes and chemically oxidized powder confirm the phase decomposition of the $LiMnBO_3$ phase when a significant amount of Li is extracted. Energy-dispersive X-ray spectroscopy and X-ray diffraction analysis also reveal Mn dissolution from the cycled $LiMnBO_3$ cathodes and chemically delithiated $LiMnBO_3$ specimen. Based on these results, we consider the cycling performance of monoclinic $LiMnBO_3$ to be primarily limited by its charged state instability. To overcome this limitation, we partially substituted Mn with Mg to maintain structural integrity of the phase and reduce capacity fading over multiple cycles.

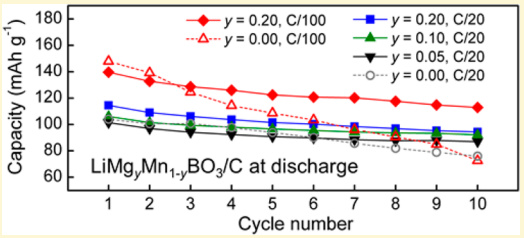

INTRODUCTION

Cathode materials containing simple polyanion groups are advantageous to cope with the growing safety concern of large-scale Li batteries: the covalent bonding within the polyanion group is believed to give these cathodes a distinctive stability against oxygen loss,[1−6] though it has been argued that this effect is not as important as believed and that for $LiFePO_4$, the good safety is more a result of the low voltage.[7,8] Among polyanionic materials, monoclinic lithium manganese borate ($LiMnBO_3$) is a system of particular interest due to its large one-electron theoretical capacity of 222 mAh g^{-1}.[9,10] However, in many studies, monoclinic $LiMnBO_3$ displays limited cycling performance with noticeable capacity fading compared to other state-of-the-art cathode materials.[10−12] Most importantly, an in-depth explanation of the major reasons for the lifetime limitation of $LiMnBO_3$ is still lacking.[10−12]

The structural stability of a cathode material, especially the stability of delithiated states, is important to understand the cycling behavior.[13−15] Although electrochemical charging and chemical delithiation of monoclinic $LiMnBO_3$ has been attempted in previous studies, the fully delithiated state could not be reached electrochemically, and amorphization occurred in preference to full oxidation.[16] In this work, we investigated the phase stability of monoclinic $LiMnBO_3$ with respect to Li contents by means of density functional theory (DFT) and compared it to X-ray diffraction patterns of electrochemically charged and chemically delithiated monoclinic $LiMnBO_3$. In the process, we suggest a possible capacity fading mechanism and also demonstrate how to further improve the material's cycling performance by partially substituting Mg for Mn. Since we are to mainly discuss monoclinic $LiMnBO_3$ in this paper, it is hereafter noted as $LiMnBO_3$ for simplicity, as the alternative hexagonal $LiMnBO_3$ polymorph is not in the scope of this investigation.

COMPUTATIONAL METHODOLOGIES

Computational results were obtained with the generalized gradient approximation and Hubbard U correction (GGA+U)[17,18] utilizing the projector augmented pseudopotential as implemented in the Vienna *Ab initio* Simulation Package (VASP).[19,20] The value of 3.9 eV is used for U to correct the d state of Mn, as determined by Wang et al.[21] Phase stability of $Li_{1-x}MnBO_3$ ($0 \leq x \leq 1$) was evaluated by constructing the 0 K quaternary phase diagram of the Li−Mn−B−O system using all the relevant compounds in the Inorganic Crystal Structure Database (ICSD) containing Li, Mn, B, and/or O.[22−24] To determine the intermediate Li-vacancy configurations for $Li_{1-x}MnBO_3$ ($0 < x < 1$), we calculated DFT energies for 20 symmetrically different Li orderings for designated x (x = 0.125, 0.5, 0.625, 0.75) and chose the lowest energy configuration as the ground state. As a reference, we also computed the energies of $Li_{1-x}FeBO_3$ ($0 \leq x \leq 1$) in a similar way.

EXPERIMENTAL PROCEDURES

Synthesis. $LiMnBO_3$ and Mg-substituted $LiMnBO_3$ ($LiMg_yMn_{1-y}BO_3$, y = 0.05, 0.1, and 0.2) were synthesized by the

Received: April 18, 2014
Revised: June 20, 2014
Published: June 30, 2014

   dx.doi.org/10.1021/cm5014174 | Chem. Mater. 2014, 26, 4200−4206

conventional solid-state method. A stoichiometric amount of Li_2CO_3 (Alfa Aesar, 99.99%), $MnC_2O_4{\cdot}2H_2O$ (Alfa Aesar, 98%), $MgC_2O_4{\cdot}2H_2O$ (Alfa Aesar, 99.9%), and H_3BO_3 (Alfa Aesar, 99.8%) was dispersed into C_2H_5O (Sigma-Aldrich, 99%) solvent and ball milled at 300 rpm for 3 days. After drying, the mixed precursor was calcined at 350 °C for 10 h under an argon atmosphere. Following intermediate manual grinding, the powder specimen was pressed into a disc-shaped pellet and fired at 500−550 °C for 10 h under an argon atmosphere. For carbon coating, 10 wt % sucrose (EMD, 99%) was added into the as-synthesized $LiMnBO_3$ and $LiMg_yMn_{1-y}BO_3$ (y = 0.05, 0.1, and 0.2) powders and was blended and ground by planetary ball milling (Retsch PM200) at a mild speed (350 rpm) for 5 h. Afterward, the mixture was annealed at 500−525 °C for 5−20 h under flowing argon. Chemically oxidized $LiMnBO_3$ was prepared by dispersing the as-synthesized $LiMnBO_3$ power into a NO_2BF_4 (Sigma-Aldrich, 95%)−CH_3CN (EMD, 99.99%) solution with a $LiMnBO_3$ to NO_2BF_4 molar ratio of 1 to 1.5 and stirring the mixture for various times at 60 °C in a sealed vessel. After rinsing with CH_3CN multiple times, the powder was dried and stored in an argon-filled glovebox.

Crystal Structure and Particle Morphology. X-ray diffraction (XRD), transmission electron microscopy (TEM), and scanning transmission electron microscopy (STEM) were performed in order to analyze the crystal structure and particle morphology. The diffraction patterns were obtained on a Rigaku diffractometer with Cu Kα and Cr Kα radiation by continuous scanning in the 2θ ranges of 18−42° and 25−65°, respectively. Rietveld refinement and profile matching of the powder diffraction data were performed with the X'pert HighScorePlus software. High-resolution (HR) TEM and STEM images were obtained under an accelerating voltage of 200 keV on a JEOL 2010F analytical electron microscope.

Elemental Analysis. Energy-dispersive X-ray spectroscopy (EDS) was taken from Helios Nanolab 600. Electron energy loss spectroscopy (EELS) from JEOL 2010F was scanned by a 0.7 nm STEM probe beam of 10.2 mrad semiconvergence angle with a step size of 0.77 nm at 2 s exposure time per spectrum and 0.5 eV per channel energy dispersion. The semicollection angle of the EELS detector is 12.3 mrad, and the inner radius of the ADF detector is 51.5 mrad. The 0.14 nm STEM imaging probe is optimized at 11.3 mrad semiconvergence angle.

Electrochemistry. The cathode consisted of 80 wt % active material, 15 wt % carbon black (Timcal, Super P), and 5 wt % polytetrafluoroethylene (PTFE; Dupont, Teflon 8C). The active material and carbon black were first mixed with a planetary ball mill for 30 min and then blended manually with PTFE in an argon-filled glovebox. A total of 1 mol of $LiPF_6$ in an ethylene carbonate (EC)−dimethyl carbonate (DMC) solution (Techno Semichem), microporous polymer film (Celgard, C480), and Li metal foil (FMC) were used as electrolyte, separator, and counter-electrode, respectively. For electrochemical measurements, a customized Swagelok-type cell was assembled inside the Ar-filled glovebox and tested on a Maccor 2200 cycler at room temperature. The loading density of the cathode was kept at approximately 3 mg/cm^2. The cathode was cycled galvanostatically at different C-rates (1 C = 222 mA g^{-1}) from 2 to 4.5 V with 1 min open circuit rest in between each charge and discharge.

RESULTS

Computed Phase Stability. Table 1 summarizes the calculated relative formation energies of $Li_{1-x}MnBO_3$ ($0 \le x \le 1$) at 0 K with respect to the ground states derived from a convex-hull construction.[24] The listed (competing) stable phases are the lowest energy states obtained from the quaternary phase diagram of the Li−Mn−B−O system.[24,25] The ΔE ("distance-to-hull") value, which scales with instability, gradually increases from 4 meV per atom at x = 0 to 140 meV per atom at x = 1.[10] The result indicates that $Li_{1-x}MnBO_3$ is thermodynamically unstable for all x. However, one may be able to regard the status of $Li_{1-x}MnBO_3$ as "relatively stable" where x < 0.625 and "relatively unstable" where $x \ge 0.625$ due to our statistical analysis that 90% of the computed energies above the convex hull for existing compounds in ICSD range from 0 to 100 meV per atom.[26]

Table 1. Computed Stability of $Li_{1-x}MnBO_3$ ($0 \le x \le 1$) and Its Ground States with Respect to Li Concentration at 0 K[a]

x in $Li_{1-x}MnBO_3$	formula	ΔE (meV/at.)	ground states
0	$LiMnBO_3$	4	h-$LiMnBO_3$
0.125	$Li_{0.875}MnBO_3$	23	h-$LiMnBO_3$, $Li_2B_4O_7$, Mn_2BO_4, Mn_3O_4
0.5	$Li_{0.50}MnBO_3$	73	h-$LiMnBO_3$, $Li_2B_4O_7$, Mn_2BO_4, Mn_3O_4
0.625	$Li_{0.375}MnBO_3$	100	$Li_3B_7O_{12}$, Mn_2BO_4, Mn_3O_4
0.75	$Li_{0.25}MnBO_3$	119	$Li_3B_7O_{12}$, MnB_4O_7, Mn_2O_3
1	$MnBO_3$	140	MnB_4O_7, MnO_2, Mn_2O_3

[a] ΔE (meV per atom) gives the difference in energy from the computed ground states. The hexagonal polymorph of $LiMnBO_3$ is denoted as h-$LiMnBO_3$.

Cycling Performance with Respect to the Depth of Charge. Figure 1a and b show representative (second) charge and discharge profiles for carbon-coated $LiMnBO_3$ ($LiMnBO_3$/C) at room temperature for two different cycling rates and the corresponding capacity retention. It is clearly seen that although a C/100 rate cycling delivers significantly larger capacities of 158 and 139 mAh g^{-1} at the second charge and discharge, respectively, than the corresponding C/20 charge and discharge cycle (112 and 102 mAh g^{-1}), its capacity fading

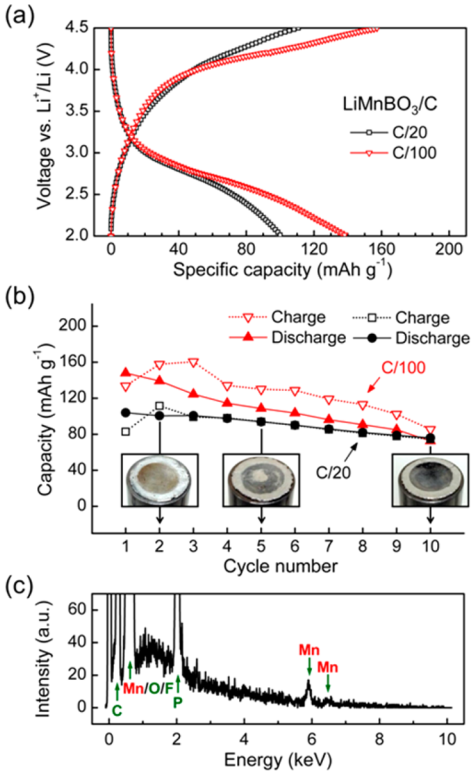

Figure 1. (a) Voltage vs capacity curves of $LiMnBO_3$/C in the second cycle at C/20 and C/100 and (b) their corresponding (dis)charge capacities for 10 cycles with photographs of a Li anode after the designated discharge cycles. (c) EDS of the stained spot on the Li anode of the cell indicates Mn deposition from the cathode during cycling. P and F originate from the soaked electrolyte salt and C and O from the EDS equipment.

dx.doi.org/10.1021/cm5014174 | Chem. Mater. 2014, 26, 4200−4206

rate of 5.1% per cycle is more severe than in C/20 cycling (2.7% per cycle). Photographs in Figure 1b show Li anodes taken from the disassembled $LiMnBO_3$/C cell after the designated C/20 discharge cycles. The coloration on the anodes intensifies as cycling number increases, and EDS of the stained spot in Figure 1c verifies that Mn is deposited on the anode during cycling.

Figure 2a shows *ex-situ* XRD patterns of $Li_{1-x}MnBO_3$/C electrodes charged to two different limits: nominal $x = 0.5$ (111

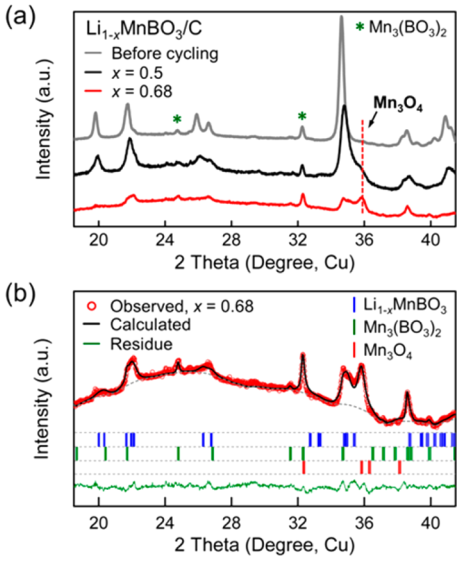

Figure 2. (a) *Ex-situ* XRD patterns of the $LiMnBO_3$/C electrodes before and after charging to two different limits: $x = 0.5$ and $x = 0.68$. (b) Profile matching of the charged $Li_{1-x}MnBO_3$/C electrode ($x = 0.68$).

mAh g^{-1}) and $x = 0.68$ (151 mAh g^{-1}). Both were prepared by C/100-rate galvanostatic charging with intermediate relaxations to ensure homogeneous Li distribution throughout the cathodes. For the highly charged sample, a peak for Mn_3O_4 is clearly visible. This is one of the decomposition products predicted in Table 1. Note that $Mn_3(BO_3)_2$ is present as an impurity phase in the specimen before cycling, and its intensity does not change significantly after undergoing charge. Identified by refining the XRD pattern of the highly charged specimen in Figure 2b, the relative ratio among the existing phases is approximately 48% $Li_{1-x}MnBO_3$, 34% Mn_3O_4, and 18% $Mn_3(BO_3)_2$.

Chemical Oxidation. To analyze the stability of the fully delithiated states, chemical oxidation was conducted. Figure 3a shows XRD patterns of pristine and chemically oxidized $LiMnBO_3$ powders. The monoclinic framework is maintained upon oxidation, although the overall peak intensity decreases. The (004) peak is seen to have shifted toward a higher angle after chemical oxidation (Figure 3a, inset). This indicates shrinkage of the *c*-lattice parameter with Li extraction from the monoclinic structure, as was also observed in $LiFeBO_3$.[27] Figure 3b shows HRTEM images of the pristine and chemically oxidized $LiMnBO_3$ particles, prepared by chemical oxidation reaction for 1.5 days. Lattice fringes are clearly observable in this chemically oxidized specimen, indicating that the particle is still crystalline. However, if the oxidation reaction continues for more than 1.5 days, the specimen abruptly transforms into an amorphous phase, as shown in Figure S1. This amorphization is

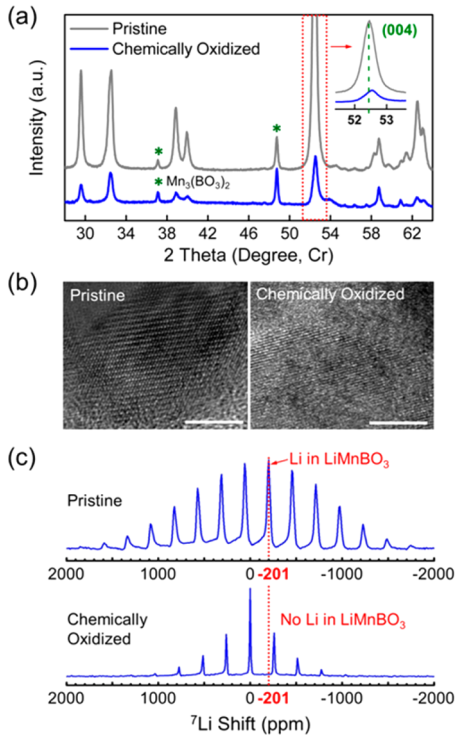

Figure 3. (a) XRD patterns, (b) HRTEM images (scale bar = 5 nm), and (c) ^{7}Li MAS NMR spectra of pristine and chemically delithiated $Li_{1-x}MnBO_3$. The NMR spectra were collected with a 1.3 mm probe (Samoson) at a magnetic field of 4.7 T, with a spinning speed of 50 kHz.

accompanied by a substantial loss in recoverable mass of the specimen, and this observation is similar to the reported result.[16] Figure 3c shows ^{7}Li magic angle spinning (MAS) nuclear magnetic resonance (NMR) spectra of pristine and chemically oxidized $LiMnBO_3$. A ^{7}Li resonance with a hyperfine shift of −201 ppm is observed in the pristine specimen, corresponding to the presence of Li in the monoclinic lithium metal borate unit cell.[28] In contrast, the chemically oxidized specimen has no such resonance at −201 ppm, suggesting that no Li remains in the original structural environment. Instead, the resonance at 0 ppm is due to diamagnetic Li-containing phases such as residual $LiBF_4$,[28] as verified by the inductively coupled plasma (ICP) results given in Table 2. Combining all

Table 2. Atomic Ratio of Elements in $LiMnBO_3$ Specimens before and after Chemical Oxidation, As Determined by Inductive Coupled Plasma (ICP, ASTM E 1097-12) and Inert Gas Fusion (ASTM E 1019-11)

chemical oxidation	atomic ratio			
before	Li	Mn	B	O
	1.07	1.01	0.97	3
after	Li	Mn	B	O
	0.38	0.63	1.55	3

the results shown in Figure 3, we conclude that fully delithiated Li_0MnBO_3 has been obtained via chemical oxidation, a phase which has never before been demonstrated.

Figure 4 shows the results of profile matching the XRD pattern obtained from the chemically oxidized $LiMnBO_3$ specimen. Using the ICSD structure of $LiMnBO_3$ (#200535), the pattern was refined with no Li present in the unit cell. Fully

dx.doi.org/10.1021/cm5014174 | Chem. Mater. 2014, 26, 4200−4206

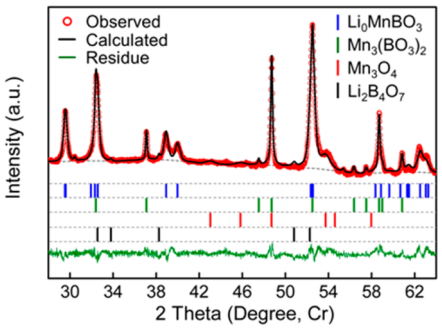

Figure 4. Profile matching of the XRD pattern of chemically oxidized $LiMnBO_3$ powder.

delithiated Li_0MnBO_3 (51 wt %) was indexed as a major phase, and $Mn_3(BO_3)_2$ (29 wt %), Mn_3O_4 (11 wt %), and $Li_2B_4O_7$ (9 wt %) were identified as minor phases in the specimen. $Mn_3(BO_3)_2$ is an impurity phase that is present even in the pristine specimen. In contrast, Mn_3O_4 and $Li_2B_4O_7$ are considered as the decomposition products of $Li_{1-x}MnBO_3$ in the process of the chemical oxidation reaction.

It is worthwhile to point out that the relative amount of $Mn_3(BO_3)_2$ in the chemically oxidized specimen is 29 wt % but less than 5 wt % in the pristine sample in Figure 3a. Since the absolute peak intensity of $Mn_3(BO_3)_2$ is unchanged before and after chemical oxidation, the result of phase identification by refinement implies that substantial amounts of $Li_{1-x}MnBO_3$ were destroyed (dissolved away) during the oxidation process. Table 2 summarizes elemental analysis results obtained from ICP and inert gas fusion for $LiMnBO_3$ powder before and after the chemical oxidation reaction. Compared to the stoichiometric Mn to O ratio in the pristine powder, Mn is deficient in the chemically oxidized specimen. Therefore, we conclude that a significant portion of Mn was dissolved into the solution during the chemical oxidation and lost in the rinsing process. This is consistent with the deposition of Mn found on the anode in electrochemical experiment. The excess Li and B contents are due to the $LiBF_4$ residual reaction byproducts, consistent with NMR results.

Partial Mg Substitution. For cathode materials that suffer from losing structural integrity during cycling, partial substitution can be an effective strategy to maintain the phase stability and to improve capacity retention.[29,30] In this context, one feasible approach to enhance the charged state stability of $LiMnBO_3$ is Fe substitution for Mn, as $LiFeBO_3$ appears to be more resistant to phase decomposition during charging, as shown through computational results presented in Table 3 and as reported experimentally by Yamada et al.[16] Structure stabilization may also be accomplished by incorporating inert elements into the host $LiMnBO_3$ framework. Mg^{2+} and Zn^{2+} can take either four- or five-fold coordination and have the proper ionic radii to reside in the trigonal bipyramidal site of Mn^{2+} in $LiMnBO_3$ and may be good candidate stabilizers.[31] Indeed, $LiMgBO_3$ and $LiZnBO_3$ are both known to form in the same monoclinic structure as $LiMnBO_3$.[22,32] However, Mg substitution is considered more suitable than Zn due to the weight advantage of Mg. The substitution amount, y, was varied between 5% and 20% to avoid compromising the theoretical capacity of $LiMg_yMn_{1-y}BO_3$.

Figure 5 shows the XRD patterns of $LiMg_yMn_{1-y}BO_3$ (y = 0, 0.05, 0.1, and 0.2) specimens fired at 500−550 °C and their lattice parameters obtained from Rietveld refinement. No

Table 3. Computed Stability of $Li_{1-x}FeBO_3$ ($0 \le x \le 1$) and Its Ground States with Respect to Li Concentration at 0 K[a]

x in $Li_{1-x}FeBO_3$	formula	ΔE (meV/at.)	ground states
0	$LiFeBO_3$	0	$LiFeBO_3$
0.125	$Li_{0.875}FeBO_3$	13	$LiFeBO_3$, Fe_3BO_5, $LiBO_2$
0.5	$Li_{0.50}FeBO_3$	42	$LiFeBO_3$, $Li_2B_4O_7$, Fe_3BO_5, $LiBO_2$, Fe_2O_3
0.625	$Li_{0.375}FeBO_3$	58	$Li_2B_4O_7$, Fe_3BO_5, $Li_3B_7O_{12}$, Fe_2O_3
0.75	$Li_{0.25}FeBO_3$	60	$Li_3B_7O_{12}$, Fe_2O_3, $Fe_2B_2O_5$, B_2O_3
1	$FeBO_3$	54	Fe_2O_3, B_2O_3

[a]The instability energy ΔE (meV per atom) gives the difference in energy from the computed ground states.

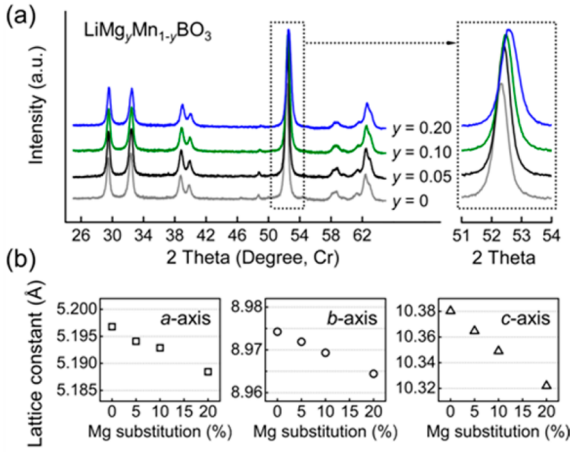

Figure 5. (a) XRD patterns of $LiMg_yMn_{1-y}BO_3$ ($0 \le y \le 0.2$) heated at 500−550 °C and (b) refined lattice parameters of these samples.

impurity peaks are detected other than one around 49° 2θ for $Mn_3(BO_3)_2$, which also existed in undoped $LiMnBO_3$ samples. As y increases, all of the lattice constants decrease, reflecting the smaller unit cell parameters of $LiMgBO_3$.[32] Thus, for all y, Mg successfully substituted for Mn and formed a solid solution.

The discharge capacities are plotted as a function of the cycle number for $LiMg_yMn_{1-y}BO_3/C$ (y = 0.05, 0.1, and 0.2) at a C/20 rate and $LiMg_{0.2}Mn_{0.8}BO_3/C$ at a C/100 rate in Figure 6. The C rate for each composition was independently based on their individual theoretical capacities of 213, 205, and 187 mAh g^{-1} for y = 0.05, 0.1, and 0.2, respectively. Mg substitution

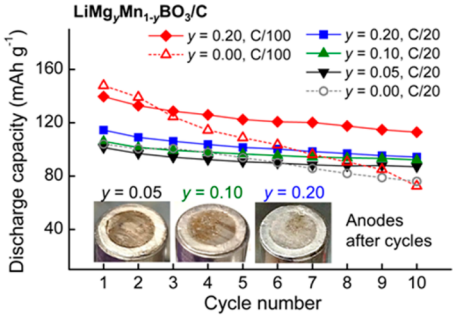

Figure 6. Discharge capacities of $LiMg_yMn_{1-y}BO_3/C$ (y = 0.05, 0.1, and 0.2) cathodes at C/20 and $LiMg_{0.2}Mn_{0.8}BO_3$ at C/100 as a function of cycle number. $LiMnBO_3$ cycled at each rate is shown for comparison. Photographic insets show the Li anodes of y = 0.05, 0.1, and 0.2 cells disassembled after 10 cycles at C/20.

dx.doi.org/10.1021/cm5014174 | Chem. Mater. 2014, 26, 4200−4206

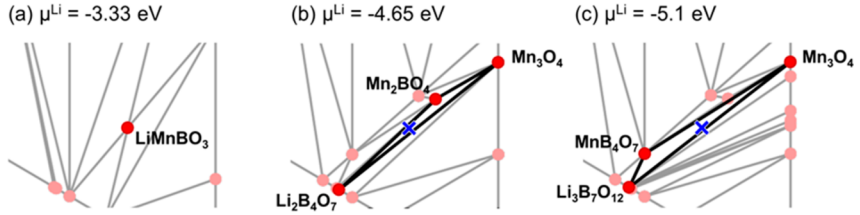

Figure 7. Graphical representation of a part of the Li grand-potential phase diagram with competing phases of $Li_{1-x}MnBO_3$ at various μ^{Li}: (a) μ^{Li} = −3.33 eV, (b) μ^{Li} = −4.65 eV, (c) μ^{Li} = −5.1 eV. Red dots stand for stable phases. $LiMnBO_3$ marked with the blue cross is unstable with respect to adjacent phases. The full phase diagrams are shown in the Supporting Information.

improves the capacity retention of $LiMnBO_3$ for all y at C/20 cycling. During 10 cycles at a C/20 rate, the discharge capacity fading rate per cycle decreased from 2.7% in $LiMnBO_3$/C to 1.4% in $LiMg_{0.05}Mn_{0.95}BO_3$/C, 1.3% in $LiMg_{0.1}Mn_{0.9}BO_3$/C, and 1.7% in $LiMg_{0.2}Mn_{0.8}BO_3$/C. At a C/100 rate, the effect of Mg substitution is more prominent: the fading rate of $LiMg_{0.2}Mn_{0.8}BO_3$/C is 1.9% per cycle, which is significantly lower than that of $LiMnBO_3$/C (5.1%). Therefore, we conclude that Mg substitution effectively enhances the capacity retention of $LiMnBO_3$/C.

DISCUSSION

Analysis of Charged State Stability. The capacity fading trend in Figure 1b can be explained by the predicted phase stability of $Li_{1-x}MnBO_3$ ($0 \le x \le 1$) in Table 1. We assume there is a threshold Li composition beyond which the structure of $Li_{1-x}MnBO_3$ collapses; this is estimated to be x = 0.625. When $LiMnBO_3$/C is cycled at a C/100 rate, the charged state can become destabilized by the large amount of Li extraction ($x \sim 0.7$). This instability is significant enough to trigger partial phase decomposition into lower energy phases, including Mn_3O_4, which is observed in the *ex-situ* XRD pattern in Figure 2. Since some amount of active mass is lost from the cathode by decomposition during charging, this leads to severe capacity fading over several cycles. In contrast, at the C/20 rate, a smaller amount of Li is extracted from $Li_{1-x}MnBO_3$. The charged state with a nominal x = 0.5 stoichiometry may not be unstable enough to drive phase decomposition, as this composition is located in the "relatively stable" regime in Table 1. For the C/20 rate cell, less capacity fading was observed with repeated cycling.

This analysis based on the computed stability can be applied to understand why $LiFeBO_3$ has better capacity retention than $LiMnBO_3$ despite sharing a common structure type. The ΔE instability values of $Li_{1-x}FeBO_3$ ($0 \le x \le 1$) in Table 3 are smaller and range from 0 to 60 meV per atom for all x, including the fully delithiated phase. As a result, all $Li_{1-x}FeBO_3$ ($0 \le x \le 1$) compositions are therefore predicted to be more stable than 50% delithiated $Li_{0.5}MnBO_3$ (ΔE = 73 meV). Therefore, the superior cycling performance of $LiFeBO_3$ compared to $LiMnBO_3$ can be attributed to the stability of the former's delithiated states.[27]

The chemical oxidation reaction drives Li extraction at a nearly constant voltage. The secondary phases observed in Figure 4, Mn_3O_4 and $Li_2B_4O_7$, can be rationalized by constructing (0 K) Li grand potential phase diagrams of the Li−Mn−B−O system as these diagrams depict the phase equilibria of the system that permits Li to flow into and out of it at a given Li chemical potential (μ^{Li}).[24,25] Figure 7 illustrates a part of the Li grand potential phase diagrams near the $LiMnBO_3$ composition at various μ^{Li}. The complete diagram is shown in the Supporting Information, Figure S2. These diagrams can also be reconstructed at the Materials Project.[33,34] Each red dot represents a stable phase, and the blue cross marks an unstable $LiMnBO_3$ composition with respect to the adjacent phases at the given μ^{Li}. In Figure 7a, $LiMnBO_3$ is seen to be a stable composition at μ^{Li} = −3.33 eV (i.e., 3.33 V vs Li^+/Li), and it remains stable at lower μ^{Li} values down to −4.64 eV. However, as μ^{Li} further decreases, $LiMnBO_3$ becomes thermodynamically unstable with respect to Mn_3O_4, $Li_2B_4O_7$, and Mn_2BO_4 at μ^{Li} = −4.65 eV (i.e., 4.65 V vs Li^+/Li) or Mn_3O_4, $Li_3B_7O_{12}$, and MnB_4O_7 at μ^{Li} = −5.1 eV (i.e., 5.1 V vs Li^+/Li). Given that the equivalent oxidation potential of the NO_2/NO_2^+ oxidizer is 5.1 V vs Li^+/Li,[35] it is possible for such predicted phases, Mn_3O_4 and $Li_2B_4O_7$, to appear during the chemical oxidation reaction. We believe the thermodynamic aspect of the computed phase diagram is well represented by the experiment.

Overall, we conclude that the delithiated state of $LiMnBO_3$ becomes unstable and loses its structural integrity due to substantial Li extraction and exposure to a highly oxidizing environment. This instability-driven phase decomposition is likely to be one of the major issues causing irreversible cycling behavior in $LiMnBO_3$. In addition, Mn dissolution is another major obstacle for capacity retention of the $LiMnBO_3$/C cathode. As shown in the photographs in Figure 1b and listed in Table 2, Mn dissolved from the cathode when $LiMnBO_3$ was severely oxidized electrochemically and chemically. As reported in Li−Mn−spinel oxides,[36−38] this Mn dissolution may be due to the chemical instability of Mn^{3+} in the charged $LiMnBO_3$ cathode in an acidic environment.

The Effects of Mg Substitution on Capacity Retention. The capacity fading rate decreases when Mg partially replaces Mn within the $LiMnBO_3$ framework, and this improved cyclability can be related to the better structural integrity of the Mg-substituted $LiMnBO_3$ cathodes. Figure 8a replots the C/100-rate cyclability data of the $LiMnBO_3$/C and $LiMg_{0.2}Mn_{0.8}BO_3$/C cathodes to compare the amount of active Li per $Mn^{2+/3+}$. Although the initial charge cycles show a similar Li activity per $Mn^{2+/3+}$, a large amount of Li per $Mn^{2+/3+}$ (>60%) is kept activated during 10 cycles for $LiMg_{0.2}Mn_{0.8}BO_3$/C in contrast to the $LiMnBO_3$/C case, in which the availability of Li per $Mn^{2+/3+}$ drops rapidly. Figure 8b shows the result of Rietveld refinement obtained from the *ex-situ* XRD of the highly charged $Li_{1-x}Mg_{0.2}Mn_{0.8}BO_3$/C electrode. The nominal state of charge was 70% (x = 0.6) based on its 187 mAh g^{-1} theoretical capacity, and the specimen was prepared by galvanostatic charging with multiple intermediate relaxations as identical to charged $Li_{1-x}MnBO_3$/C in Figure 2. Although the Mn_3O_4 product is observed again, the estimated relative phase composition of the specimen is 62.9% of $Li_{1-x}Mg_{0.2}Mn_{0.8}BO_3$, 23.8% of Mn_3O_4, and 13.2% of

dx.doi.org/10.1021/cm5014174 | *Chem. Mater.* 2014, 26, 4200−4206

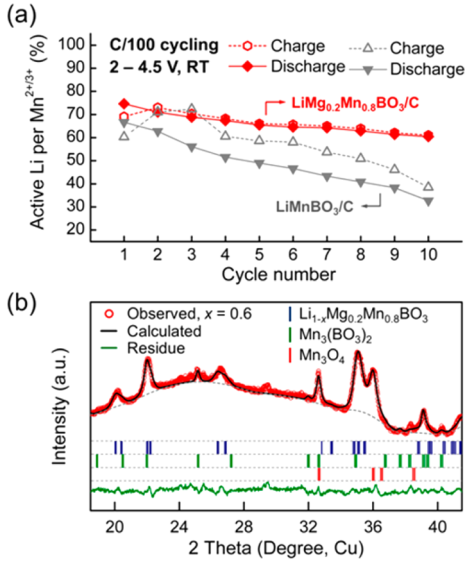

Figure 8. (a) Utilization of Li per $Mn^{2+/3+}$ over multiple cycles and (b) Rietveld refinement of the charged $Li_{1-x}Mg_{0.2}Mn_{0.8}BO_3/C$ electrode (x = 0.6).

$Mn_3(BO_3)_2$. The ratio of Mn_3O_4 to the monoclinic main phase decreased substantially in the charged $Li_{1-x}Mg_{0.2}Mn_{0.8}BO_3/C$ cathode, as compared to the undoped case in Figure 2b, which suggests that Mg substitution reduces the phase decomposition at the highly charged state. Hence, we demonstrate that Mg serves as a structural stabilizer to lessen the degree of phase decomposition when a large amount of Li is extracted.

The coloration on the Li anodes from the disassembled $LiMg_yMn_{1-y}BO_3$ (y = 0.05, 0.1, and 0.2) cells in Figure 6 was not as visible as in Figure 1b, suggesting that Mg substitution also minimizes Mn dissolution. According to the HRTEM and STEM images of the charged $Li_{1-x}Mg_{0.2}Mn_{0.8}BO_3/C$ particle in Figure 9a and b, an amorphous layer approximately 2-nm-thick appears at the surface of the crystalline particle. Figure 9c shows 16 electron energy loss spectra taken along the arrow in Figure 9b and the corresponding intensity ratios of boron and manganese or oxygen in these EELS spectra. The ratio from the spectra 12−15 highlighted in the red section of Figure 9b reveals that the amorphous layer is boron-rich compared to the crystalline particle. Note that the EELS edge for C is also detected in this layer. Therefore, STEM-EELS analysis shown in Figure 9 was used to verify that a uniform boron-rich layer had formed on the $LiMg_{0.2}Mn_{0.8}BO_3/C$ particle along with the carbon coating. However, as no such layer was observed in $LiMnBO_3$ (data not shown), the boron-rich layer is believed to have effectively protected the particle surface from dissolution and improved cyclability. The layer likely prevents the aggressive reaction between $LiMg_{0.2}Mn_{0.8}BO_3$ and the electrolyte at the particle surface by introducing a protective coating, which can help to reduce Mn dissolution.

Although the overall performance of the $LiMnBO_3/C$ cathode and its Mg-substituted derivatives still require further enhancement to be considered as practical Li intercalation cathodes, we were able to make significant progress to better understand the cycling behavior and identify the major limiting factor of the material for reversible Li storage. Moreover, the capacity fading rate of 1.3% per cycle in $LiMg_{0.1}Mn_{0.9}BO_3/C$ is a substantial improvement compared to the previously reported $LiMnBO_3$ cathodes.[10−12] Based on this work, we expect that with further efforts to stabilize $Li_{1-x}MnBO_3$ by substitution and the addition of improved protective layer coatings, further improvements in the electrochemical properties can be achieved for $LiMnBO_3$-based cathodes.

CONCLUSION

In summary, we conclude that the thermodynamic stability of $LiMnBO_3$ decreases significantly during the process of Li extraction, as predicted by first-principles calculations. Decomposition products from *ex-situ* XRD on the charged electrode and on chemically oxidized powder demonstrated the instability of the charged state of $LiMnBO_3$. The charged state instability leads to actual losses in the active mass by phase decomposition and Mn dissolution. Instability of the charged state is therefore a major limiting factor of the electrochemical performance of $LiMnBO_3$. These processes can be mitigated when $LiMnBO_3$ is stabilized by Mg substitution. $LiMg_yMn_{1-y}BO_3$ ($0.05 \leq y \leq 0.2$) showed improved cyclability due to reduced phase decomposition and Mn dissolution. We believe Mg effectively serves as a structural stabilizer that supports the host framework at the charged state and induces formation of a boron-rich surface layer that minimizes the parasitic electrolyte−electrode reaction at the particle surface.

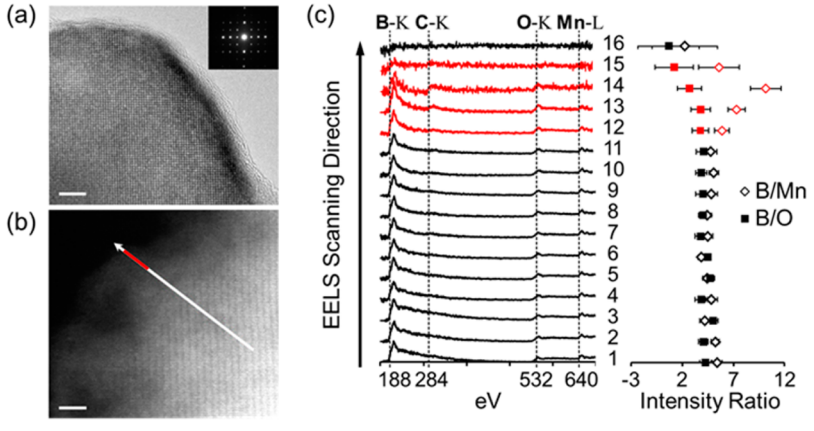

Figure 9. (a) HRTEM image (scale bar: 5 nm) and electron diffraction pattern along the [100] zone axis and (b) STEM image (scale bar: 2 nm) of the $LiMg_{0.2}Mn_{0.8}BO_3$ particle and (c) 16 STEM-EELS profiles and intensity ratios of B/Mn and B/O along the arrow in b, which indicates the EELS scanning direction and range.

dx.doi.org/10.1021/cm5014174 | *Chem. Mater.* 2014, 26, 4200−4206

■ ASSOCIATED CONTENT

Supporting Information

The XRD pattern and HRTEM image of chemically oxidized $LiMnBO_3$ powder (for 10 days) and Li grand potential phase diagrams of the Li−Mn−B−O system at μ^{Li} = −3.33, −4.65, and −5.1 eV. This material is available free of charge via the Internet at http://pubs.acs.org.

■ AUTHOR INFORMATION

Corresponding Author

*E-mail: gceder@mit.edu.

Notes

The authors declare no competing financial interest.

■ ACKNOWLEDGMENTS

This work was supported in part by the MRSEC Program of the National Science Foundation under award number DMR-0819762 and by the Assistant Secretary for Energy Efficiency and Renewable Energy, Office of Vehicle Technologies of the U.S. Department of Energy under Contract No. DE-AC02-05CH11231, under the Batteries for Advanced Transportation Technologies (BATT) Program. Computing resources were provided through the National Energy Research Scientific Computing Center (NERSC) and from the Extreme Science and Engineering Discovery Environment (XSEDE) under grant number TG-DMR970008S. The Materials Project work is supported by Department of Energy's Basic Energy Sciences program under Grant No. EDCBEE, DOE Contract DE-AC02-05CH11231. Collaborative NMR characterization experiments at Stony Brook University were supported by the Northeastern Center for Chemical Energy Storage, an Energy Frontier Research Center funded by the U.S. DOE, BES under award no. DE-SC0001294. This work was also supported in part by Robert Bosch GmbH and Umicore Specialty Oxides and Chemicals.

■ REFERENCES

(1) Padhi, A. K.; Nanjundaswamy, K. S.; Goodenough, J. B. *J. Electrochem. Soc.* **1997**, *144*, 1188.
(2) Masquelier, C.; Padhi, A. K.; Nanjundaswamy, K. S.; Goodenough, J. B. *J. Solid State Chem.* **1998**, *135*, 228.
(3) Legagneur, V.; An, Y.; Mosbah, A.; Portal, R.; La Salle, A. L.; Verbaere, A.; Guyomard, D.; Piffard, Y. *Solid State Ionics* **2001**, *139*, 37.
(4) Nyten, A.; Abouimrane, A.; Armand, M.; Gustafsson, T.; Thomas, J. O. *Electrochem. Commun.* **2005**, *7*, 156.
(5) Seo, D. H.; Kim, H.; Park, I.; Hong, J.; Kang, K. *Phys. Rev. B* **2011**, *84*, No. 220106(R).
(6) Goodenough, J. B.; Park, K. S. *J. Am. Chem. Soc.* **2013**, *135*, 1167.
(7) Hautier, G.; Jain, A.; Mueller, T.; Moore, C.; Ong, S. P.; Ceder, G. *Chem. Mater.* **2013**, *25*, 2064.
(8) Ceder, G. *MRS Bull.* **2010**, *35*, 693.
(9) Seo, D. H.; Park, Y. U.; Kim, S. W.; Park, I.; Shakoor, R. A.; Kang, K. *Phys. Rev. B* **2011**, *83*, No. 205127.
(10) Kim, J. C.; Moore, C. J.; Kang, B.; Hautier, G.; Jain, A.; Ceder, G. *J. Electrochem. Soc.* **2011**, *158*, A309.
(11) Lee, Y. S.; Lee, H. *J. Ceram. Process. Res.* **2012**, *13*, S237.
(12) Afyon, S.; Kundu, D.; Krumeich, F.; Nesper, R. *J. Power Sources* **2013**, *224*, 145.
(13) Darling, R.; Newman, J. *J. Electrochem. Soc.* **1998**, *145*, 990.
(14) Winter, M.; Besenhard, J. O.; Spahr, M. E.; Novak, P. *Adv. Mater.* **1998**, *10*, 725.
(15) Tarascon, J. M.; Armand, M. *Nature* **2001**, *414*, 359.
(16) Yamada, A.; Iwane, N.; Nishimura, S.; Koyama, Y.; Tanaka, I. *J. Mater. Chem.* **2011**, *21*, 10690.
(17) Perdew, J. P.; Burke, K.; Ernzerhof, M. *Phys. Rev. Lett.* **1996**, *77*, 3865.
(18) Dudarev, S. L.; Botton, G. A.; Savrasov, S. Y.; Humphreys, C. J.; Sutton, A. P. *Phys. Rev. B* **1998**, *57*, 1505.
(19) Kresse, G.; Furthmuller, J. *Phys. Rev. B* **1996**, *54*, 11169.
(20) Kresse, G.; Joubert, D. *Phys. Rev. B* **1999**, *59*, 1758.
(21) Wang, L.; Maxisch, T.; Ceder, G. *Phys. Rev. B* **2006**, *73*, No. 195107.
(22) Bondareva, O. S.; Simonov, M. A.; Egorovtismenko, Y. K.; Belov, N. V. *Sov. Phys. Crystallogr.* **1978**, *23*, 269.
(23) Bergerhoff, G.; Hundt, R.; Sievers, R.; Brown, I. D. *J. Chem. Inf. Comput. Sci.* **1983**, *23*, 66.
(24) Ong, S. P.; Wang, L.; Kang, B.; Ceder, G. *Chem. Mater.* **2008**, *20*, 1798.
(25) Mo, Y. F.; Ong, S. P.; Ceder, G. *Chem. Mater.* **2012**, *24*, 15.
(26) Wu, Y. B.; Lazic, P.; Hautier, G.; Persson, K.; Ceder, G. *Energy Environ. Sci.* **2013**, *6*, 157.
(27) Yamada, A.; Iwane, N.; Harada, Y.; Nishimura, S.; Koyama, Y.; Tanaka, I. *Adv. Mater.* **2010**, *22*, 3583.
(28) Bo, S. H.; Wang, F.; Janssen, Y.; Zeng, D. L.; Nam, K. W.; Xu, W. Q.; Du, L. S.; Graetz, J.; Yang, X. Q.; Zhu, Y. M.; Parise, J. B.; Grey, C. P.; Khalifah, P. G. *J. Mater. Chem.* **2012**, *22*, 8799.
(29) Prasad, R.; Benedek, R.; Thackeray, M. M. *Phys. Rev. B* **2005**, *71*, No. 134111.
(30) Lu, W.; Belharouak, I.; Park, S. H.; Sun, Y. K.; Amine, K. *Electrochim. Acta* **2007**, *52*, 5837.
(31) Shannon, R. D. *Acta Crystallogr., Sect. A* **1976**, *32*, 751.
(32) Norrestam, R. *Z. Kristallogr.* **1989**, *187*, 103.
(33) Jain, A.; Ong, S. P.; Hautier, G.; Chen, W.; Richards, W. D.; Dacek, S.; Cholia, S.; Gunter, D.; Skinner, D.; Ceder, G.; Persson, K. A. *APL Mater.* **2013**, *1*, No. 011002.
(34) The Materials Project Homepage. https://www.materialsproject.org.
(35) Wizansky, A. R.; Rauch, P. E.; Disalvo, F. J. *J. Solid State Chem.* **1989**, *81*, 203.
(36) Amatucci, G. G.; Blyr, A.; Sigala, C.; Alfonse, P.; Tarascon, J. M. *Solid State Ionics* **1997**, *104*, 13.
(37) Cho, J. P.; Kim, T. J.; Kim, Y. J.; Park, B. *Chem. Commun.* **2001**, 1074.
(38) Du Pasquier, A.; Blyr, A.; Courjal, P.; Larcher, D.; Amatucci, G.; Gerand, B.; Tarascon, J. M. *J. Electrochem. Soc.* **1999**, *146*, 428.